Influence of offshore fringing reefs on infragravity period oscillations within a harbor

Junliang Gao[1, 2 *], Xiaojun Zhou[1], Jun Zang[2], Qiang Chen[2], Li Zhou[1 *]

1 School of Naval Architecture and Ocean Engineering, Jiangsu University of Science and Technology, Zhenjiang 212003, China

2. Research Unit for Water, Environment and Infrastructure Resilience (WEIR), Department of Architecture and Civil Engineering, University of Bath, BA2 7AY, U.K.

Abstract

The main objective of this paper is to systematically study the influence of offshore fringing reef topography on the infragravity-period harbor oscillations under the condition of wave breaking occurring over the reef. The infragravity (IG) period oscillations inside an elongated harbor excited by bichromatic wave groups are simulated using a fully nonlinear Boussinesq model. Based on a wave analysis technique, influences of plane reef-face slope, reef-face profile shape and reef ridge on the maximum IG period component amplitude, the bound and the free IG waves and their relative components inside the harbor are comprehensively investigated. Results show that under the condition of wave breaking occurring over the reef, all the four above-mentioned variables increase gradually with the reef-face slope, and tend to increase first, then decrease, and then increase again with the mean water depth over the reef face. For the reef-face profile shapes with relatively large mean water depth (equal to or larger than 3.0 m), the existence of the reef ridge always significantly enhances the bound IG waves inside the harbor, while its influences on the maximum IG period component amplitude and the free IG waves both depend on the incident primary wave amplitudes.

Key words:

Harbor oscillations; Fringing-reef topography; Wave breaking; Bound infragravity waves; Free infragravity waves; Fully nonlinear Boussinesq models

* Corresponding author. E-mail: gaojunliang880917@163.com (J. Gao), zhouli209@hotmail.com (L. Zhou).

1. Introduction

Infragravity (IG) period waves are surface gravity waves with periods between 30 s and 5 min and wave lengths between 100 m and 10 km (Rabinovich, 2009). Via nonlinear wave-wave interactions, the IG period waves can be generated and propagate beneath the primary (short) wave groups (Longuet-Higgins and Stewart, 1962). When the IG period waves with frequencies close to those of resonating harbor modes come into a harbor entrance, they can be highly amplified into inner basins and cause large oscillations of the water surface (Bowers, 1977). Although other external forces can also excite significant oscillations within a harbor, which include atmospheric pressure fluctuations (De Jong and Battjes, 2004), shear flows (Fabrikant, 1995), tsunamis (Gao et al., 2017a; Gao et al., 2018) and impact waves induced by landslides or the failure of structures near the harbor (Dong et al., 2010), for most harbors around the world (where the surface water area is about 1–10 km^2 and the depth is about 5–10 m), the most common external force may be the IG period waves mainly generated through nonlinear interaction of primary wave groups. By creating unacceptable vessel movements, harbor oscillations may interrupt cargo handling, disturb operational efficiency and generate excessive mooring forcing that may break mooring lines (Kumar et al., 2016).

González-Marco et al. (2008) studied the influences of the IG period waves on harbor operations in Gijón Port (Spain) and found that if the IG period waves are present in the wave trains, the port's inactivity time is significantly increased, although very good protection against short wind waves is provided by the harbor. Similar situations were also observed in many other ports and harbors, such as Pohang New Harbor in South Korea (Kumar et al., 2014), Marina di Carrara harbor in Italy (Guerrini et al., 2014), Two Rocks Marina in Australia (Thotagamuwage and Pattiaratchi, 2014), Port of Ferrol in Spain (López and Iglesias, 2013) and Paradip Port in India (Kumar and Gulshan, 2017). Therefore, to relieve the disturbance to harbor operation and minimize possible destructive effects, further research efforts are essential to enhance our present knowledge for the IG period oscillations and thus improve our forecasting ability for the potential adverse effects.

Dong et al. (2013) proposed an IG wave analysis technique to decompose the IG period components inside the harbor into bound and free IG waves, and by using a Boussinesq model, further investigated the influences of the short wavelength on the bound and the free IG waves and

their relative components inside the harbor when the lowest resonant mode, which was induced by bichromatic wave groups, occurred. Subsequently, Gao et al. (2016a) extended the study of Dong et al. (2013) to the lowest four modes, and the effects of not only the short wavelength but also the incident short wave amplitude on IG period waves inside the harbor were systematically investigated. For these two papers, the water depths inside and outside the harbor were set to a constant, and the influence of the offshore topography on harbor oscillations was not considered. Recently, given that the offshore fringing reefs can raise the IG wave energy towards the nearshore and remarkably strengthen the IG period oscillations inside the harbor (Thotagamuwage and Pattiaratchi, 2014), Gao et al. (2017b) further systematically studied the influences of the fringing reefs on the bound and the free IG waves and their relative components inside the harbor when the lowest mode was induced by bichromatic wave groups. Subsequently, Gao et al. (2017c) expanded the investigations of Gao et al. (2017b) to the second to the fifth modes. Although the research findings in Gao et al. (2017b) and Gao et al. (2017c) improved the knowledge on the influence of offshore fringing reefs on the IG period oscillations inside the harbor to some degree, both of them adopted relatively small incident wave amplitudes and wave breaking did not occur over the offshore fringing reefs. In fact, because the water depth over offshore fringing reefs is often very shallow, the phenomenon of wave breaking can be frequently observed (Dong et al., 2014; Nwogu and Demirbilek, 2010; Thotagamuwage and Pattiaratchi, 2014; Yao et al., 2016; Yao et al., 2018). Hence, the studies of Gao et al. (2017b) and Gao et al. (2017c) need to be further expanded to consider wave breaking over the fringing reef.

To enhance the understanding of the IG period waves inside the harbor that is involved in IG period oscillations and offshore reef topographies, this article further studies how the maximum IG period component amplitude, the bound and the free IG waves and their relative components vary with respect to the topographic variation over the offshore fringing reef. Identical to Gao et al. (2017b), investigations in current paper are only confined to the lowest resonant mode induced by bichromatic primary wave groups with two slightly different frequencies. However, different from Gao et al. (2017b), the amplitudes of the incident bichromatic primary waves adopted in this paper are much larger, which leads to the occurrence of wave breaking over the offshore fringing reef. The similarities and differences of wave hydrodynamics inside the harbor under the two conditions of with and without considerations of wave breaking are comprehensively compared

and discussed in this paper. All simulations in this article are implemented by using a fully nonlinear Boussinesq model. For simplification, the harbor is assumed to be long and narrow, and then the free surface movement inside the harbor essentially becomes one dimensional.

The remainder of the paper is organized as follows: Section 2 briefly introduces the numerical model and the analysis technique. The applicability of the numerical model for wave motions over the fringing reef under the condition of wave breaking will be verified by experimental data. Section 3 presents the numerical experiment setup and the experimental wave parameters. Section 4 illustrates the simulation results, which are explained in detail. Concluding remarks based on the results are shown in Section 5.

2. Numerical model and analysis technique

2.1. Numerical model

2.1.1. Model description

All numerical experiments in this article are carried out by using the famous and widely implemented FUNWAVE 2.0 model. It was proposed and developed at the University of Delaware (Kirby et al., 2003). The governing equations in this model are based on the fully nonlinear Boussinesq equations derived by Wei et al. (1995). Shi et al. (2001) subsequently discretized the equations on the staggered grid in generalized curvilinear coordinates for a better fit for irregularly shaped shorelines. The one-way wave generating method proposed by Chawla and Kirby (2000) is adopted to create monochromatic or random waves. Sponge layers are installed at the boundaries of the computational domain to effectively dissipate the energy of outgoing waves with various directions and frequencies. Some additional terms are added in the momentum conservation equation to represent the effects of wave breaking, bottom friction and subgrid lateral turbulent mixing. The coefficients related to these additional terms include two breaking-related parameters, C_{br} and δ_b, the bed friction coefficient f_b and the subgrid mixing coefficient C_m (the explanation of these coefficient can be seen in Kirby et al. (2003) and the references therein), and can be adjusted based on existing physical experiments. The capability of the model to predict wave propagation and transformation from deep to shallow water has been well validated by laboratory experiments (Kirby et al., 2003; Ma et al., 2017).

To verify the ability of the FUNWAVE 2.0 model to simulate harbor oscillations with strong wave nonlinearity inside the harbor, Gao et al. (2016b) employed the model to reproduce the

physical experiments carried out by Rogers and Mei (1978). Gao et al. (2016b) compared the numerical results of the first three super harmonics with the experimental data of Rogers and Mei (1978) for two elongated rectangular bays of different lengths. Overall agreement was observed between the measured data and the numerical results for all the three super harmonics. It was shown that the numerical model can also simulate strong nonlinear harbor oscillations accurately.

2.1.2. Model validation for wave motions over the fringing reef

To further verify the applicability of the FUNWAVE 2.0 model on the simulation of wave transformations and wave energy evolution over fringing coral reefs, the model is used to reproduce the laboratory experiments of Nwogu and Demirbilek (2010). The experiments were implemented with a reef profile typical of fringing reef systems along the southeast coast of Guam in a two-dimensional wind-wave flume at the University of Michigan. The flume is 35 m long, 0.7 m wide and 1.6 m high. The reef cross section consisted of a 1:12 beach followed by a 4.8-m-wide reef flat and a composite-slope reef face as shown in Fig. 1 and was built using polyvinyl chloride plastic. Irregular waves were generated in the tank with a plunger-type wavemaker. Tests were run for a wide variety of irregular wave conditions with significant wave heights varying from 3.0 to 8.5 cm, spectral peak periods from 1.0 to 2.5 s, and water depth h_I from 0 to 5.0 cm on reef flat. Time histories of the water surface elevation were synthesized from JONSWAP spectral shapes with peak enhancement factor γ=3.3 using random phase method. The experimental results were recorded at nine wave gauges shown in Fig. 1. The locations of these wave gauges are x= –1.11, –0.92, –0.59, 2.75, 3.68, 4.22, 4.80, and 9.14 m from the toe of the reef. The test that we select herein has the incident wave conditions of significant wave height of H_S=0.075 m, spectral peak wave period of T_p=1.5 s and water depth h_I=3.1 cm in the reef flat. In numerical simulations, the computational domain is slightly shorter than the flume in the experiments. The domain length is 28.5 m, discretized by 570 grids with Δx=0.05 m. To obtain a good convergence rate, the maximum Courant number $C_r = (gh_0)^{1/2}\Delta t/\Delta x$ is required to be less than 0.5, in which h_0=0.531 m denotes the water depth over the open sea. Therefore, we use a time step of Δt=0.01 s in all simulations. A 10.0-m-wide sponge layer is placed behind the internal wavemaker to effectively absorb seaward-propagating long waves.

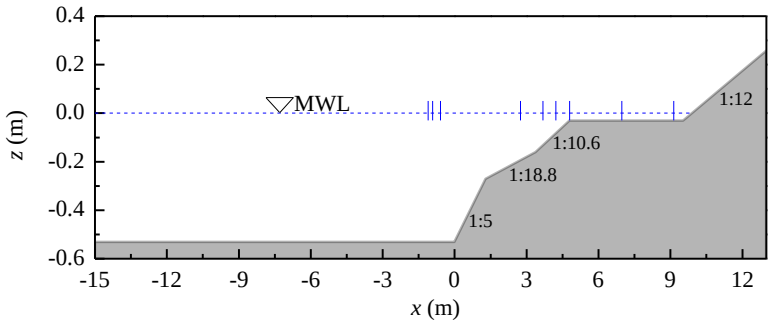

Fig. 1. The computational domain and reef topography for the flume experiment of Nwogu and Demirbilek (2010). The solid blue lines demonstrate the locations of nine wave gauges (gauge 1 to gauge 9 from left to right). The water depth at the reef flat is h_I=3.1 cm.

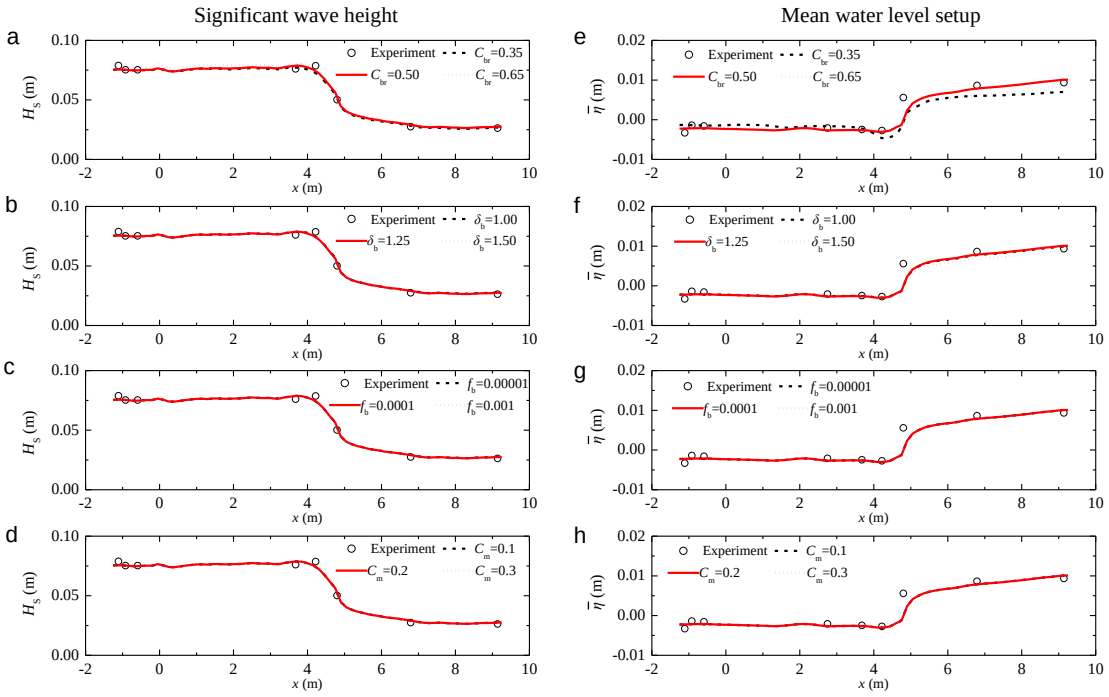

Fig. 2. Sensitivity analyses of the parameters, C_{br}, δ_b, f_b and C_m, for (a–d) significant wave height variation and (e–h) mean water level setup for the experiment of Nwogu and Demirbilek (2010) (incident wave conditions: H_S=0.075 m, T_p=1.5 s, h_I=3.1 cm)

As has been mentioned in Section 2.1.1, in the FUNWAVE 2.0 model, C_{br}, δ_b, f_b and C_m are a set of adjustable parameters which may affect the simulation results. Hence, the sensitivity analyses of these parameters should be performed first to assess their influences on the simulation results. In fact, for the above four parameters, Kirby et al. (2003) recommended the value range of each parameter. For C_{br}, δ_b, f_b and C_m, their typical value ranges are 0.35–0.65, 1.0–1.5, 0.00001–

0.001 and 0.1–0.3, respectively. Fig. 2 illustrates the measured and model-predicted significant wave height variation and mean water level setup across the reef-slope topography for different values of C_{br}, δ_b, f_b and C_m. The significant wave height is calculated based on Rayleigh wave height distribution $H_S = 4\sigma_\eta$, where σ_η is the standard deviation of free surface. The sensitivity analyses of C_{br} for the significant wave height variation and the mean water level setup are carried out first (Fig. 2a and e). Three different values of C_{br} (i.e., 0.35, 0.50 and 0.65) are selected with constant values of δ_b =1.25, f_b=0.0001 and C_m=0.2. It is seen that for both the significant wave height variation and the mean water level setup, C_{br}=0.50 gives the best agreement between the measured and predicted data. Then, the sensitivity analyses of δ_b are implemented (Fig. 2b and f). Three different values of δ_b (i.e., 1.00, 1.25 and 1.50) are selected with constant values of C_{br}=0.50, f_b=0.0001 and C_m=0.2. For the significant wave height variation, the three values of δ_b produce almost identical numerical results, which agree with the measured data very well. While, for the mean water level setup, δ_b =1.25 yields the best agreement between the measured and predicted data. Next, the sensitivity analyses of f_b are performed (Fig. 2c and g). Three different values of f_b (i.e., 0.00001, 0.0001 and 0.001) are selected with constant values of C_{br}=0.50, δ_b=1.25 and C_m=0.2. For both the significant wave height variation and the mean water level setup, the three different values of f_b produce almost identical numerical results, and these results agree well with the measured data, overall. At last, the sensitivity analyses of C_m are carried out (Fig. 2d and h). Three different values of C_m (i.e., 0.1, 0.2 and 0.3) are selected with constant values of C_{br}=0.50, δ_b=1.25 and f_b =0.0001. Similar to Fig. 2c and g, for both the significant wave height variation and the mean water level setup, the three different values of C_m produce almost identical numerical results, and these results also agree well with the measured data, overall. Based on the above analyses, the numerical results obtained with the values of C_{br}=0.50, δ_b=1.25, f_b=0.0001 and C_m=0.2 show the best agreement with the measured data. To show this phenomenon more intuitively, the numerical results obtained with C_{br}=0.50, δ_b=1.25, f_b=0.0001 and C_m=0.2 and their comparisons with the measured data are demonstrated separately in Fig. 3.

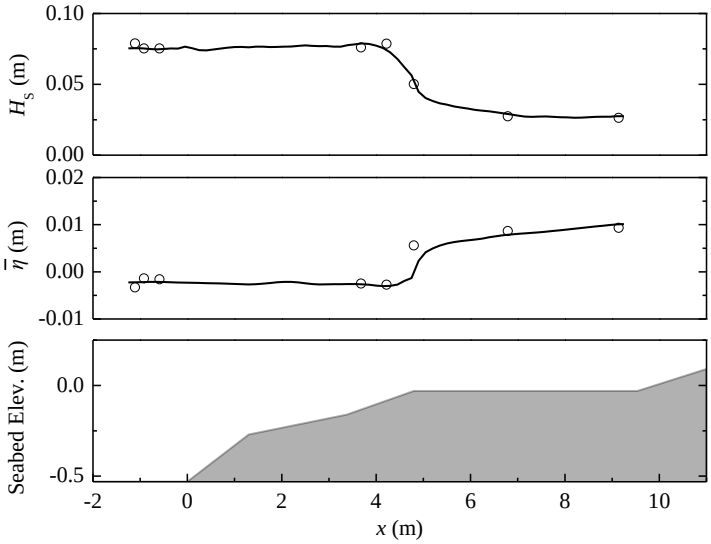

Fig. 3. Comparisons of measured and predicted significant wave height and mean water level setup for the experiment of Nwogu and Demirbilek (2010) (incident wave conditions: H_S=0.075 m, T_p=1.5 s, h_I=3.1 cm) under the conditions of C_{br}=0.50, δ_b=1.25, f_b=0.0001 and C_m=0.2

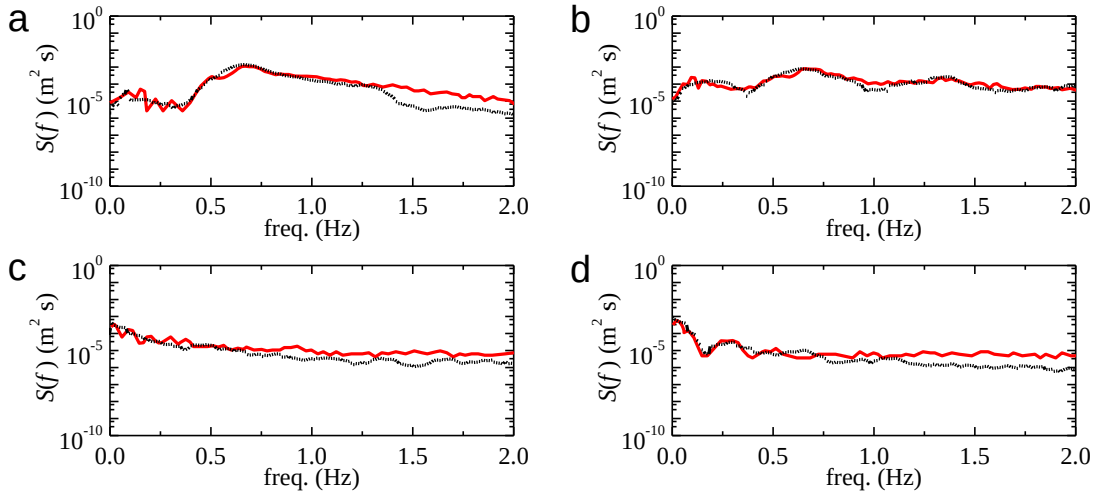

Fig. 4. Comparisons of simulated (black lines) and measured (red lines) wave spectra at (a)gauge 3, (b) gauge 6, (c) gauge 8 and (d) gauge 9 for the experiment of Nwogu and Demirbilek (2010) (incident wave conditions: H_S=0.075 m, T_p=1.5 s, h_I=3.1 cm) under the conditions of C_{br}=0.50, δ_b=1.25, f_b=0.0001 and C_m=0.2

Fig. 4 compares the simulated and measured wave energy spectra at gauges 3, 6, 8 and 9 under the conditions of C_{br}=0.50, δ_b=1.25, f_b=0.0001 and C_m=0.2. As seen in Fig. 1, gauge 3 is located in the offshore, gauge 6 is in the reef slope, while gauges 8 and 9 are situated at the middle

and end of the reef flat, respectively. Although the reef face is a relatively complicated composite slope, the evolution of wave energy spectrum from offshore to the reef flat involving the generation of IG waves is well captured by the model. At gauges 3, 8 and 9 (Fig. 4a, c and d), the energy density at high frequency band (f >1.0 Hz) is slightly underestimated. Considering the relatively low wave energy at this frequency band, this underestimation would not affect the wave height distribution significantly. From this benchmark, we can conclude that the FUNWAVE 2.0 model is capable of simulating nonlinear wave processes in the reef environment when the values of the four adjustable parameters are properly chosen.

Based on the above sensitivity analyses of the four adjustable parameters for simulation results, the values of C_{br}=0.50, δ_b=1.25 and C_m=0.2 are adopted in our numerical experiments that will be described in detail in Section 3. However, the bed friction coefficient f_b will be set to zero in the following simulations. The reason lies on that the current study only focuses on the influence of offshore fringing reef topography on the IG period harbor oscillations. The topographic variations of the fringing reef include different plane reef-face slopes, various reef-face profile shapes and whether the reef ridge exists or not. If the bottom friction was considered in the simulations, the simulation results would not be purely affected by the topographic variation of the fringing reef, and would be inevitably influenced by the bottom friction. Besides, there is one more reason for not considering the bottom friction in this paper. As has been mentioned in the Introduction, Gao et al. (2017b) investigated the influence of offshore fringing reef topography on the IG period harbor oscillations without considering wave breaking over the reef. In order to correctly compare similarities and differences of wave hydrodynamics inside the harbor under the two conditions of with and without considerations of wave breaking, except for the incident primary wave amplitudes that can control whether waves break or not over the reef, all the other factors that may affect the simulation results should be kept identical to Gao et al. (2017b). Since the bottom friction was not considered in Gao et al. (2017b), it should not be considered in current study as well.

2.2. Analysis technique

In this paper, the IG wave analysis technique that was first proposed by Dong et al. (2013) is adopted to decompose the IG period components inside the harbor into the bound and the free IG waves. This wave analysis technique started from a theoretical solution of the free surface

elevation of the IG period waves inside a long and narrow rectangular harbor exposed to bichromatic primary wave groups, which was first deduced and formulated by Bowers (1977). After some mathematical treatments, the squared amplitude of the IG period component inside the harbor was represented as the summation of three basis functions. By equidistantly deploying a series of wave gauges along the center line of the harbor, the squared amplitude of the IG period component could be directly obtained from the free surface signals by applying the discrete Fourier transform technology. Then, by using the least squares method, the amplitudes of the bound and the free IG waves and their initial phase difference could be calculated. For the more detailed descriptions of this IG wave analysis technique, the interested reader is referred to Dong et al. (2013). Its capability to decompose the bound and the free IG waves inside the harbor for various resonant modes have been fully validated by Dong et al. (2013) and Gao et al. (2016a).

3. Numerical experimental setup

Due to similar research purposes with Gao et al. (2017b) and meanwhile in order to facilitate the comparisons of the similarities and differences of wave hydrodynamics inside the harbor under the two conditions of with and without considerations of wave breaking, the numerical experimental setup in this paper is set to be almost identical to that in Gao et al. (2017b) except in the following three aspects. Firstly, because wave breaking is considered in current study, the incident primary wave amplitudes adopted in this paper are much larger than those in Gao et al. (2017b). Secondly, in this paper, in order to judge whether wave breaking occurs over the reef or not, wave gauges are arranged not only inside the harbor but also over the reef. Thirdly, to reduce the computational cost, the total simulation time for all simulations decreases from 2000.0 s in Gao et al. (2017b) to 1200.0 s in this paper, and its rationality will be explained in Section 4.1. To enhance the reader's understanding of this article and facilitate the descriptions of the results that will be demonstrated in Section 4, the numerical experimental setup is briefly described in this section although many details are similar to those in Gao et al. (2017b).

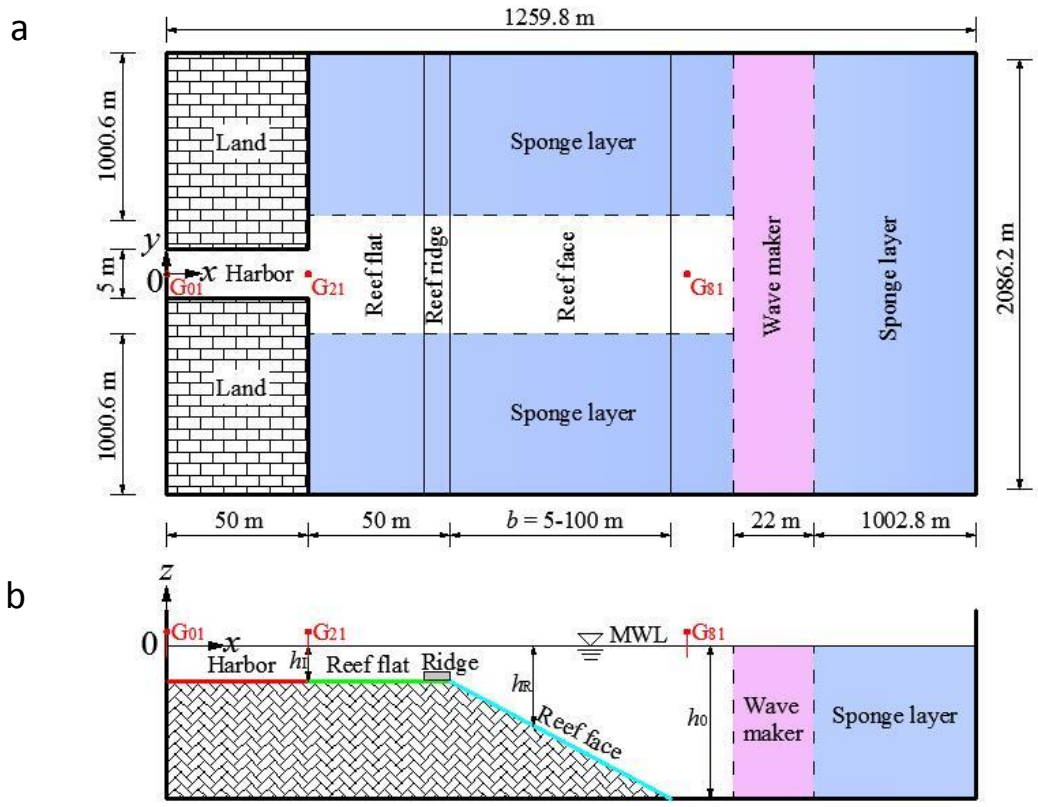

Fig. 5. Sketch of the numerical experimental setup: (a) top view; (b) longitudinal section at y=0 (taking the reef face with the plane slope for example).

Fig. 5 demonstrates the numerical wave tank used in all simulations. The wave tank has dimensions of 1259.8 m by 2086.2 m, and the harbor has a length of 50.0 m and a width of 5.0 m. All the edges of the wave tank and the harbor are represented by perfectly reflecting vertical walls. The reef flat located outside the harbor has a length of 50.0 m. The width of the reef face, b, increases gradually from 5.0 m to 100.0 m in interval of 5.0 m. Eighty-one wave gauges (G_{01}–G_{81}) are arranged equidistantly along the center line of the wave tank with a spacing of 2.5 m, among which twenty-one wave gauges (G_{01}–G_{21}) are deployed inside the harbor. The abscissa values of gauges G_{01}, G_{21} and G_{81} are x=0, 50.0 and 200.0 m, respectively. The water depth inside the harbor and over the reef flat is equal to h_1=1.0 m, and the water depth over the open sea is h_0=5.0 m. Based on the theoretical solution for the oscillations inside the elongated rectangular harbor (Mei, 1983), the eigenfrequencies of the lowest five resonant modes of the harbor shown in Fig. 5 are computed and listed in Table 1. In this article, only the lowest mode excited by bichromatic wave groups with two slightly different frequencies is investigated. The frequencies of the

incident primary waves are set to f_1=0.250 Hz and f_2=0.264 Hz, so that the beat frequency, $\Delta f=|f_1-f_2|$, coincides with the eigenfrequency of the lowest mode. Different from Gao et al. (2017b), to ensure wave breaking occurring over the fringing reef, the following four different incident primary wave amplitudes are considered: (1) $a_1=a_2$=0.12 m, (2) $a_1=a_2$=0.14 m, (3) $a_1=a_2$=0.16 m and (4) $a_1= a_2$=0.18 m, in which a_1 and a_2 denote the amplitudes of the incident f_1 and f_2 wave components, respectively. In addition, to study the effects of the reef ridge on the IG period waves inside the harbor, two idealized reef profiles are considered: (1) a fringing reef with an idealized ridge and (2) a fringing reef without a ridge. For the former, a rectangular box with dimensions of 2086.2 m×6.0 m×0.3 m is positioned on the reef flat with its front face aligned to the reef edge (x=100.0 m) to imitate an idealized ridge. Both the seaside and the leeside vertical faces of the ridge are altered to a slope of S=0.6 to ensure the numerical stability in simulations. To effectively dissipate the energy of the reflected and radiated waves with various directions and frequencies, sponge layers are deployed at the right, bottom and upper boundaries of the wave tank. To save the computational time, only half of the domain (i.e. $y \geq 0$) is utilized as the computational domain for all simulations due to the geometric symmetry with respect to the center line of the wave tank. In the x-direction, the grid sizes Δx are all equal to 0.5 m except in the sponge layer at the right boundary; in the sponge layer, they increase gradually from 0.5 m to 18.7 m to lower the large computational cost related to the very large sponge layer width. In the y-direction, the grid sizes Δy gradually increase from 0.5 m inside the harbor to 19.9 m outside the harbor. A time step of Δt=0.025 s and a total simulation time of 1200.0 s are used in all numerical experiments.

Table 1. Theoretical solution (Mei, 1983): eigenfrequencies, f (Hz), and amplification factors, $R(f)$, of the lowest five modes for the harbor shown in Fig. 5.

	Resonant mode				
	I	II	III	IV	V
f	0.014	0.043	0.073	0.103	0.133
R(f)	14.35	4.83	2.98	2.21	1.77

Identical to Gao et al. (2017b), to mimic different reef-face profiles, three types of profiles

(i.e., plane slope bottom, arc-tangent-type bottom and hyperbolic-cosine-type bottom) are adopted, and the still water depths over these three types of reef-face profiles are given by

$$h_{\mathrm{R}}(x)=\begin{cases} h_{\mathrm{I}}+S(x-100) & \text{Plane slope bottom} \\ h_{\mathrm{I}}+\alpha\operatorname{atan}\left[\beta(x-100)\right] & \text{Arc-tangent-type bottom} \\ h_{\mathrm{I}}\cosh^{\kappa}\left[\mu(x-100)\right] & \text{Hyperbolic-cosine-type bottom} \end{cases} \tag{1}$$

S, α, β, κ and μ are parameters that determine the bottom profile over the reef face, which conform to the following relationships:

$$S=\frac{h_0-h_{\mathrm{I}}}{b}, \tag{2}$$

$$\beta=\frac{1}{b}\tan\left(\frac{h_0-h_{\mathrm{I}}}{\alpha}\right), \tag{3}$$

and

$$\mu=\frac{1}{b}\operatorname{acosh}\left[\left(\frac{h_0}{h_{\mathrm{I}}}\right)^{1/\kappa}\right]. \tag{4}$$

Although for the plane slope bottom profile, the reef-face width, b, increases gradually from 5.0 m to 100.0 m in interval of 5.0 m, for both the arc-tangent-type and hyperbolic-cosine-type bottom profiles, only the cases with b=50.0 m and 100.0 m are simulated. Table 2 demonstrates the geometric parameters of the various reef-face profiles adopted in all simulations. $\bar{h}_{\mathrm{R}}$ in this table denotes the mean water depth over the reef face, and is calculated by:

$$\bar{h}_{\mathrm{R}}=\frac{1}{b}\int_{100}^{100+b}h_{\mathrm{R}}(x)dx. \tag{5}$$

To intuitively show the shape differences of the various topographies listed in Table 2, the comparisons of these bottom profiles with the reef-face width b=50.0 m are demonstrated in Fig. 6. For the reef faces with b=100.0 m, the topographies for the various bottom profiles are identical to those illustrated in this figure except that the reef-face width is doubled.

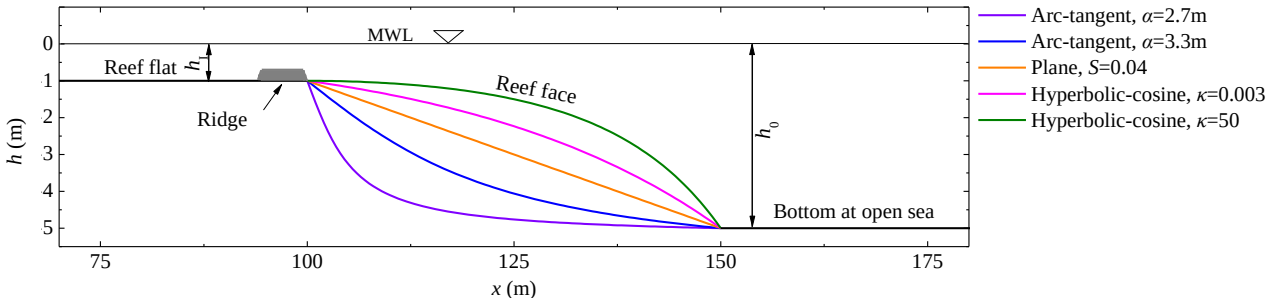

Fig. 6. Comparison of the various reef-face profiles with the reef-face width b=50.0 m

Table 2. Geometric parameters for the various reef-face profiles

Topography	Geometric parameters	
Plane	b=5.0 m–100.0 m, S=0.80–0.04, $\bar{h}_R$ =3.00 m	
Arc-tangent-type	b=50.0 m	α=2.7 m, $\bar{h}_R$ =4.42 m
		α=3.3 m, $\bar{h}_R$ =3.70 m
	b=100.0 m	α=2.7 m, $\bar{h}_R$ =4.42 m
		α=3.3 m, $\bar{h}_R$ =3.70 m
Hyperbolic-cosine-type	b=50.0 m	κ=0.003, $\bar{h}_R$ =2.48 m
		κ=50.0, $\bar{h}_R$ =1.94 m
	b=100.0 m	κ=0.003, $\bar{h}_R$ =2.48 m
		κ=50.0, $\bar{h}_R$ =1.94 m

4. Results and discussion

4.1. Time series and wavelet analysis

Time series and corresponding wavelet spectra of the free surface elevations at gauge G_{01} for different incident primary wave amplitudes under the conditions of b=50.0 m, plane reef face and no reef ridge are presented in Figs. 7 and 8, respectively. Note that in Fig. 7, the time series of the free surface elevations at gauge G_{01} are normalized by the average incident primary wave amplitudes, $a=(a_1a_2)^{1/2}$. Fig. 7 shows that the free water surface inside the harbor is calm at the initial period of time. The incident primary waves reach the position of gauge G_{01} at about 60 s for all the four cases. Via the wavelet spectra illustrated in Fig. 8, the wave energy variation with respect to the frequency and the time can be visually demonstrated. The energy of the primary wave components rises from zero to their maximum levels very rapidly (about 60.0 s) and then remains steady until the end of the simulation. However, more time is needed for the IG period components to attain the quasi-steady state from the initial response phase. For both the four cases, the IG period components reach the quasi-steady state at about t=300.0 s. In this article, only the quasi-steady processes (i.e., the free surface signals from t=300.0 s to t=1200.0 s) are investigated in all simulations. Via a simple calculation, it is shown that the quasi-steady processes are approximately 13 times the period of the IG components, which is long enough to obtain steady and reliable analysis results. Hence, it is reasonable that the total simulation time for all simulations is shorten from 2000.0 s in Gao et al. (2017b) to 1200.0 s in this paper.

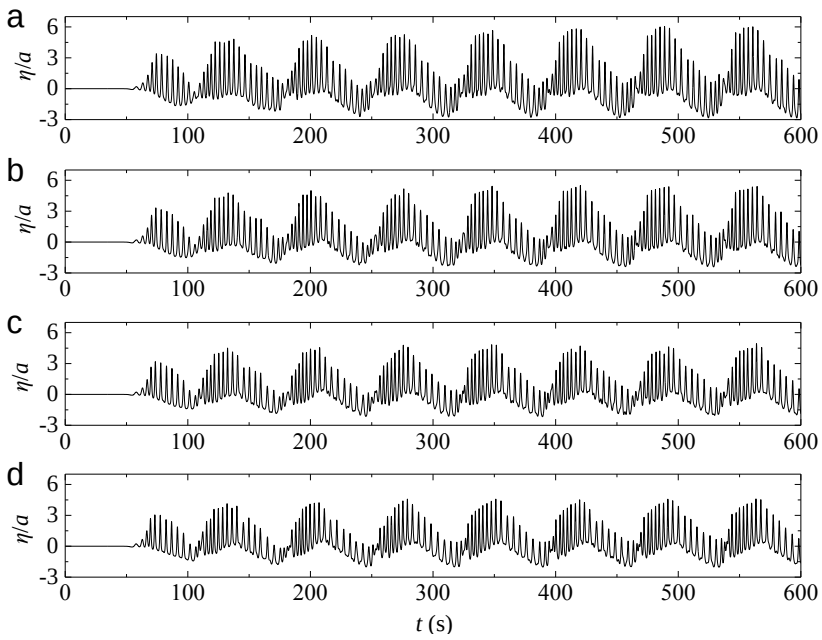

Fig. 7. Time series of the free surface elevations at gauge G_{01} for (a) a_1=a_2=0.12 m, (b) a_1=a_2=0.14 m, (c) a_1=a_2=0.16 m and (d) a_1=a_2=0.18 m under the conditions of b=50.0 m, plane reef face and no reef ridge, in which a=$(a_1a_2)^{1/2}$.

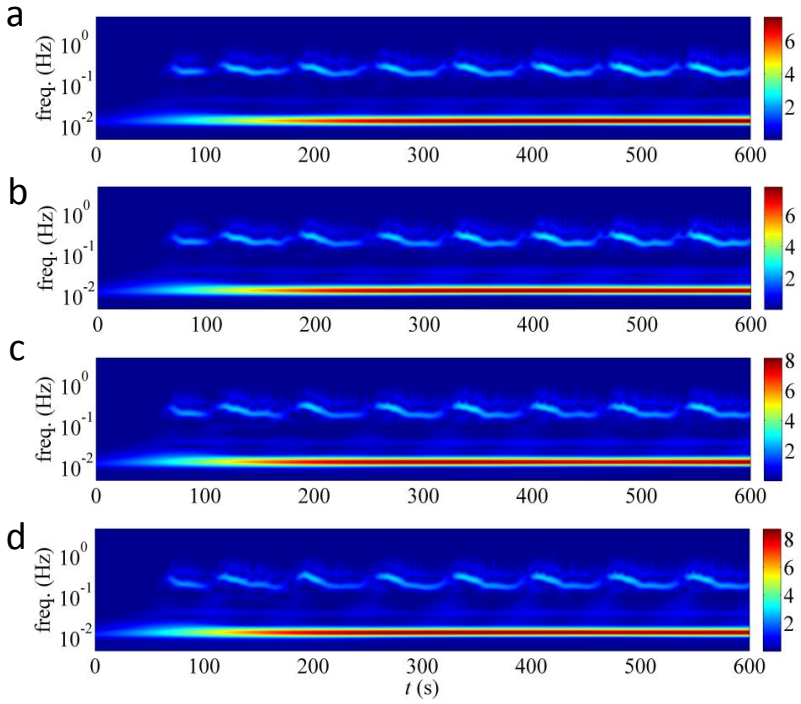

Fig. 8. Wavelet spectra at gauge G_{01} for (a) a_1=a_2=0.12 m, (b) a_1=a_2=0.14 m, (c) a_1=a_2=0.16 m and (d) a_1=a_2=0.18 m under the conditions of b=50.0 m, plane reef face and no reef ridge

4.2. Wave amplitude evolutions over the fringing reef

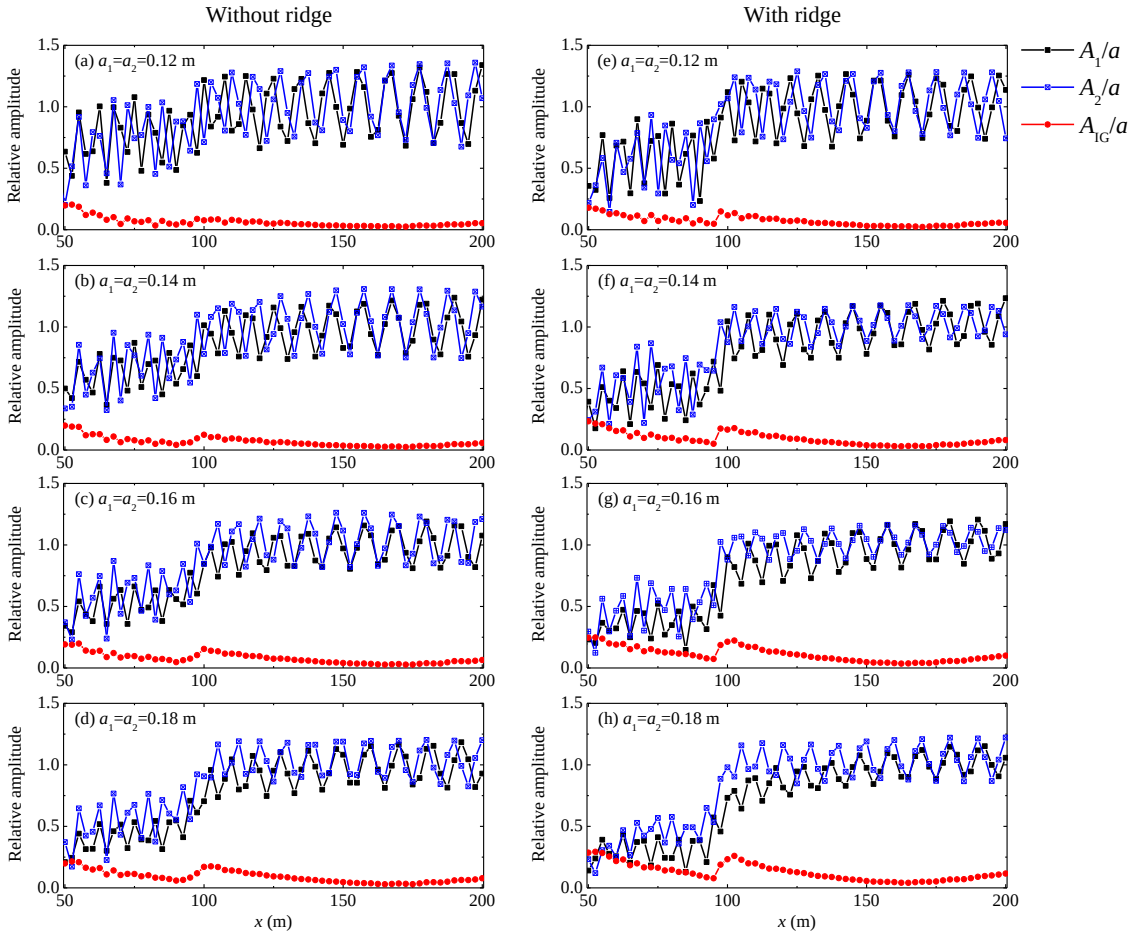

Fig. 9. Wave amplitude evolutions of primary waves and IG period waves over the fringing reef along the *x*-axis for different incident primary wave amplitudes under the conditions of *b*=50.0 m and plane reef face. (a)–(d) correspond to the cases without the ridge, and (e)–(h) correspond to the cases with the ridge.

Prior to utilizing the IG wave separation procedure described in Section 2.2 to decompose the IG period components inside the harbor into bound and free IG waves, it is necessary to examine whether wave breaking occurs over the reef under the conditions of the four incident primary wave amplitudes considered in this paper. Fig. 9 demonstrates the wave amplitude evolutions of primary waves and IG period waves over the fringing reef along the *x*-axis for different incident primary wave amplitudes under the conditions of *b*=50.0 m and plane reef face. When the reef-face width *b*=50.0 m, the reef flat and the reef face are located at the ranges of 50.0<x≤ 100.0

m and 100.0<x≤150.0 m, respectively, while the region with x>150.0 m is the open sea. From this figure, it is clearly seen that for all the four incident primary wave amplitudes considered in this paper, both the primary waves and the IG period waves show the characteristics of standing waves due to the wave energy reflection over the fringing reef and from the shoreline. For the primary wave amplitudes, there is an obvious decrease in the vicinity of the reef edge (x=100.0 m) along the inshore direction, no matter whether the reef ridge exists or not. Besides, the larger the incident primary wave amplitudes are, the more obvious this downward trend becomes. These phenomena indicate that for all the four incident primary wave amplitudes considered in this paper, wave breaking occurs near the reef edge; the larger the incident primary wave amplitudes are, the more intense wave breaking becomes. For the amplitudes of the IG period wave components, there also exists an obvious fluctuation near the reef edge. The larger the incident primary wave amplitudes are, the more obvious this fluctuation becomes. From this figure, it also can be found that for both the primary waves and the IG period waves, their amplitude fluctuations near the reef edge with the reef ridge (Fig. 9e–h) are always larger than those without the reef ridge (Fig. 9a–d), which indicates that the existence of the reef ridge intensifies wave breaking that occurs near the reef edge.

4.3. Effect of the reef-face slope on IG period waves

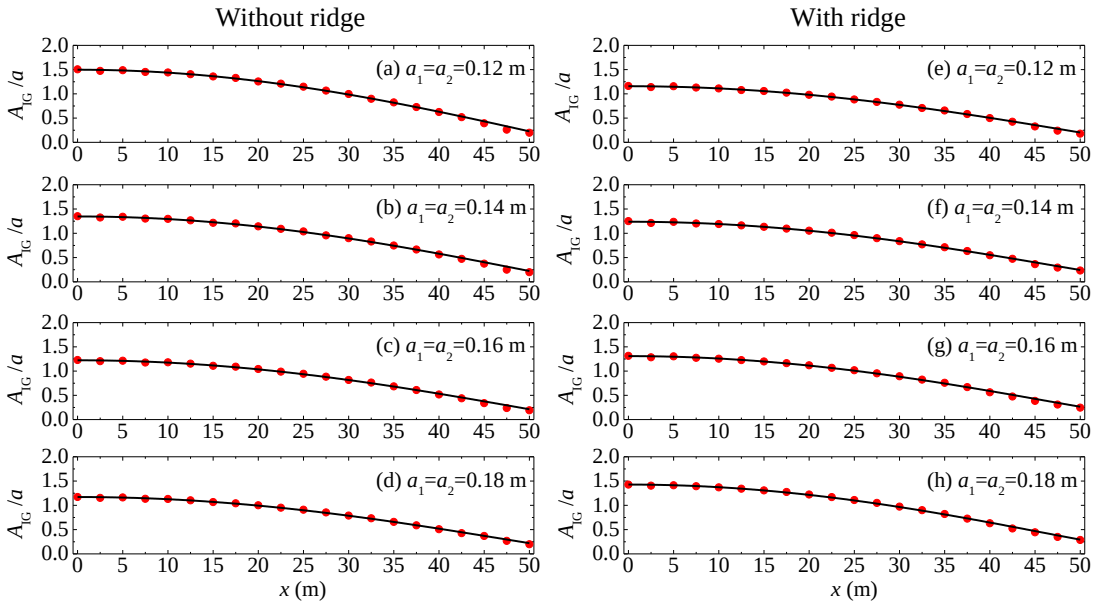

Fig. 10. Amplitudes of the IG period components (red dots) at all wave gauges inside the harbor and their fitted envelopes (black lines) obtained using the wave analysis technique for different

incident primary wave amplitudes under the conditions of b=50.0 m and plane reef face. (a)–(d) correspond to the cases without the ridge, and (e)–(h) correspond to the cases with the ridge.

Table 3. The separation results of the bound and the free IG wave components for the eight cases shown in Fig. 10. A_m in this table denotes the maximum IG period component amplitude inside the harbor, which corresponds to the IG wave amplitudes at gauge G_{01}. ζ_b and ζ_f denote the amplitudes of the bound and the free IG waves, respectively, and α_b and α_f denote their respective initial phases.

Case	Results				
	A_m (m)	ζ_b (m)	ζ_f (m)	$\lvert\alpha_b-\alpha_f\rvert$ (°)	ζ_b/ζ_f (%)
(a)	1.81×10^{-1}	1.93×10^{-2}	1.67×10^{-1}	49.97	11.60
(b)	1.90×10^{-1}	3.59×10^{-2}	1.88×10^{-1}	94.59	19.11
(c)	1.97×10^{-1}	4.22×10^{-2}	2.03×10^{-1}	105.9	20.79
(d)	2.11×10^{-1}	7.43×10^{-2}	2.33×10^{-1}	116.4	31.89
(e)	1.39×10^{-1}	3.30×10^{-2}	1.45×10^{-1}	106.9	22.78
(f)	1.75×10^{-1}	6.57×10^{-2}	1.99×10^{-1}	121.7	33.06
(g)	2.10×10^{-1}	9.12×10^{-2}	2.45×10^{-1}	123.1	37.23
(h)	2.57×10^{-1}	1.17×10^{-1}	3.04×10^{-1}	124.4	38.70

Employing the IG wave analysis technique shown in Section 2.2, the bound and the free IG standing wave components inside the harbor are decomposed in all simulations. Fig. 10 demonstrates the amplitudes of the IG period components in all wave gauges and their fitted envelopes obtained by utilizing the analysis technique for different incident primary wave amplitudes under the conditions of b=50.0 m and plane reef face. It is seen that the amplitudes of the IG period components at all wave gauges are very close to their fitted envelopes in all the eight cases, which indicates that the separating amplitudes of the bound and the free IG wave components are accurate and reliable. Table 3 presents the separation results of the eight cases. In this table, A_m denotes the maximum IG period component amplitude inside the harbor, which corresponds to the IG wave amplitudes at gauge G_{01}; ζ_b and ζ_f respectively denote the amplitudes of the bound and the free IG waves, and α_b and α_f refer to their respective initial phases. For the eight cases, although the values of ζ_b and ζ_f are different from each other, the values of ζ_b/ζ_f are all less than 100%, which indicates that the bound IG wave components inside the harbor are always

less than the free IG wave components in these cases. From Fig. 10, it also can be observed that for all the eight cases, the maximum IG period component amplitude inside the harbor always appears at the backwall of the harbor where gauge G_{01} is placed. The phenomenon is accordance with the findings in the previous relevant studies (i.e., Dong et al. (2013); Gao et al. (2017b)) in which the lowest resonant mode was investigated. For the reef faces with different plane slopes, the variations of the maximum IG period component amplitude inside the harbor, A_m, with respect to the slope coefficient, S^{-1}, under the conditions of different incident primary wave amplitudes are demonstrated in Fig. 11. It can be observed that for both the two conditions of with and without the reef ridge, the maximum IG period component amplitude inside the harbor increases gradually with the increasing of the reef-face slope, S, and the larger the incident primary wave amplitudes are, the more obvious this variation trend becomes. For the condition of with the reef ridge (Fig. 11b), the above-mentioned phenomena are particularly obvious.

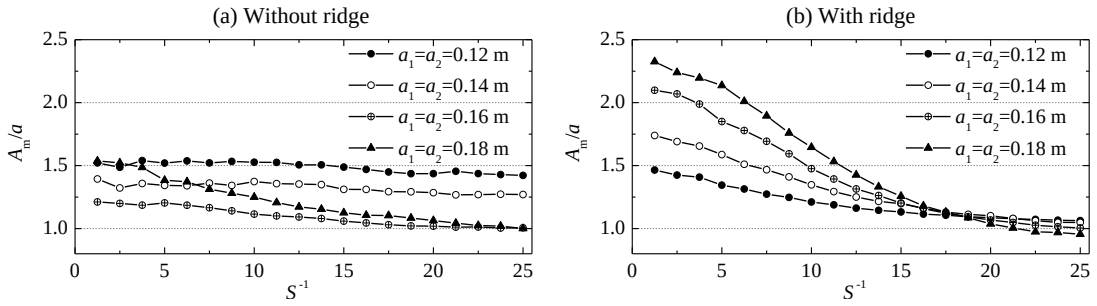

Fig. 11. Variations of the maximum IG period component amplitude inside the harbor, A_m, with respect to the slope coefficient, S^{-1}, under the conditions of different incident primary wave amplitudes. (a) and (b) correspond to the cases without and with the reef ridge, respectively.

The variations of the separating amplitudes of the bound and the free IG waves with respect to the slope coefficient, S^{-1}, under the conditions of different incident primary wave amplitudes are presented in Fig. 12. It can be observed that for all the four incident primary wave amplitudes considered in this paper, the reef-face slope has a remarkable influence on both the bound and the free IG waves inside the harbor. Identical to the maximum IG period component amplitude inside the harbor, the amplitudes of both the bound and the free IG waves also increase gradually with the increasing of the reef-face slope, S. It should be noted here that for the free IG waves inside

the harbor, their variation trend found in this paper is identical to that found in Gao et al. (2017b). However, for the bound IG waves inside the harbor, their variation trend in this paper is remarkably different from that in Gao et al. (2017b) who pointed out that when wave breaking does not occur over the fringing reef, the bound IG waves inside the harbor is insensitive to the variation of the reef-face slope. Besides, it also can be observed that for all the cases shown in this figure, the amplitudes of the free IG waves are always larger than those of the bound IG waves inside the harbor, which agrees with the findings in Dong et al. (2013) and Gao et al. (2017b). It is attributed to that the free IG waves inside the harbor correspond to the lowest resonant modes and are remarkably amplified.

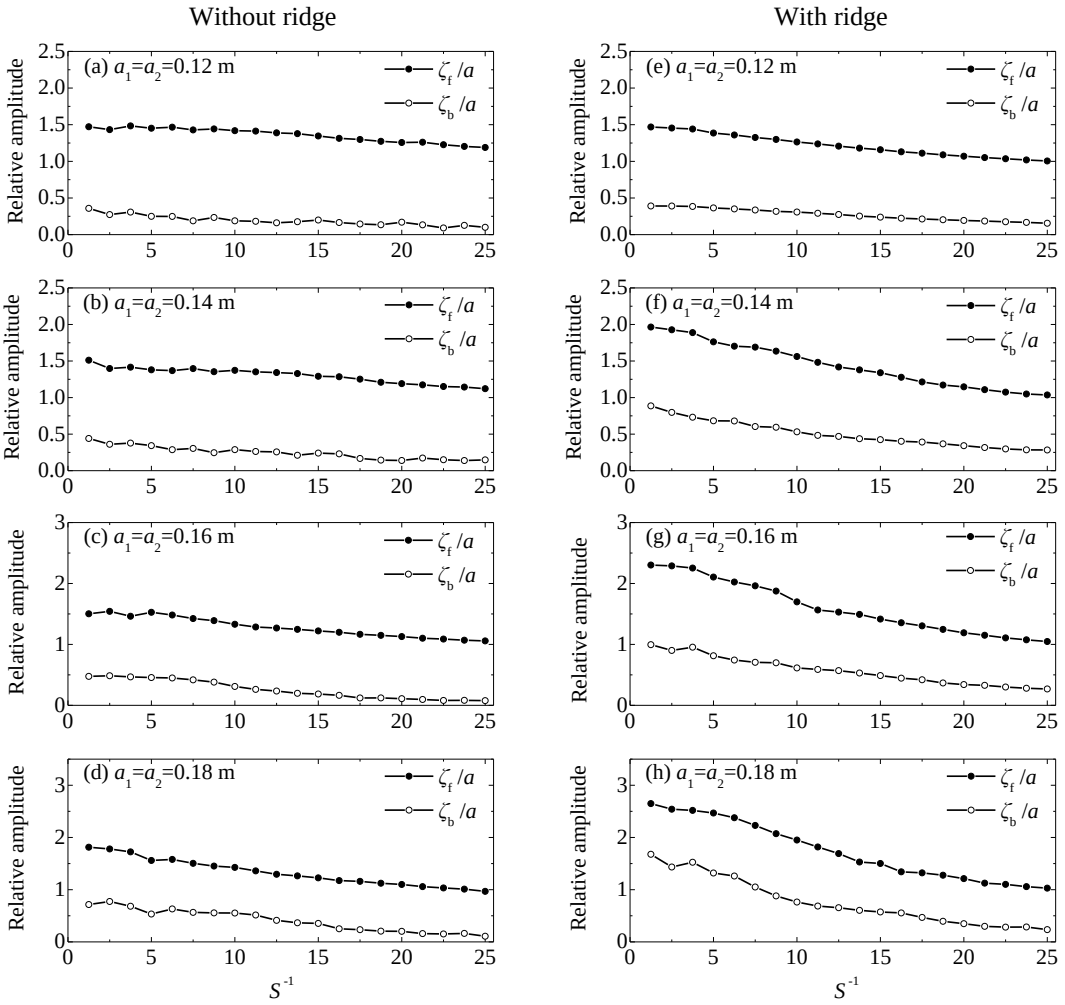

Fig. 12. Variations of the separating amplitudes of the bound and the free IG waves with respect to the slope coefficient, S^{-1}, under the conditions of different incident primary wave amplitudes. (a)–(d) correspond to the cases without the ridge, and (e)–(h) correspond to the cases with the ridge.

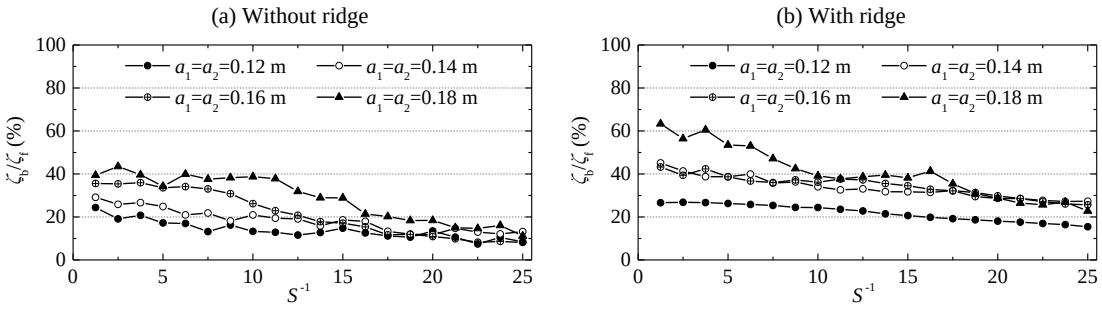

Fig. 13. The amplitude ratios, ζ_b / ζ_f, for all the cases with different plane reef-face slopes. (a) and (b) correspond to the cases without and with the reef ridge, respectively.

Fig. 13 shows the variation of the amplitude ratio, ζ_b/ζ_f, with respect to the slope coefficient, S^{-1}, for different incident primary wave amplitudes. It can be seen that similar to the phenomenon shown in Figs. 11 and 12, in general, the amplitude ratio, ζ_b/ζ_f, always increases with the increasing of the reef-face slope, S, regardless of the incident primary wave amplitudes and whether the reef ridge exists or not. This variation trend of the amplitude ratio found in this paper is diametrically opposed to the corresponding findings in Gao et al. (2017b).

4.4. Effect of the shape of reef-face profile on IG period waves

To study effects of different topographies over the reef face on the maximum IG period component amplitude and the bound and the free IG wave components inside the harbor, five different bottom profile shapes, as shown in Fig. 6, under the conditions of b=50.0 m and 100.0 m are considered. Fig. 14 shows the variations of the maximum IG period component amplitude, the separating amplitudes of the bound and the free IG waves and their relative components with respect to the mean water depth over the reef face, $\bar{h}_R$, under the condition of b=50.0 m. Different from the findings in Gao et al. (2017b) that under the condition of b=50.0 m, the free IG wave amplitude always increases monotonically with the increasing of $\bar{h}_R$, and both the bound IG wave amplitude and the amplitude ratio, ζ_b/ζ_f, decrease monotonically with the increasing of $\bar{h}_R$, it can be observed from Fig. 14 that all the four variables shown in this figure generally have a similar variation trend. That is, all of them tend to increase first, then decrease, and then increase again with the increasing of the mean water depth over the reef face, $\bar{h}_R$, regardless of the incident primary wave amplitudes and whether the reef ridge exists or not. Besides, in general, all the four

variables get the maximum and minimum values when $\bar{h}_R$ =2.48 m and $\bar{h}_R$ =3.00 m, respectively. This phenomenon indicates that the reef face with plane slope can lead to minimum IG period components inside the harbor (including minimum A_m, ζ_b and ζ_f), compared to the other four topographies shown in Fig. 6; while the hyperbolic-cosine-type reef face with κ=0.003 can lead to maximum IG period components inside the harbor (including maximum A_m, ζ_b and ζ_f). Hence, from the viewpoint of the practical engineering application, the reef face with plane slope can restrain the IG period components inside the harbor to the most extent, compared to other profile shapes over the reef face.

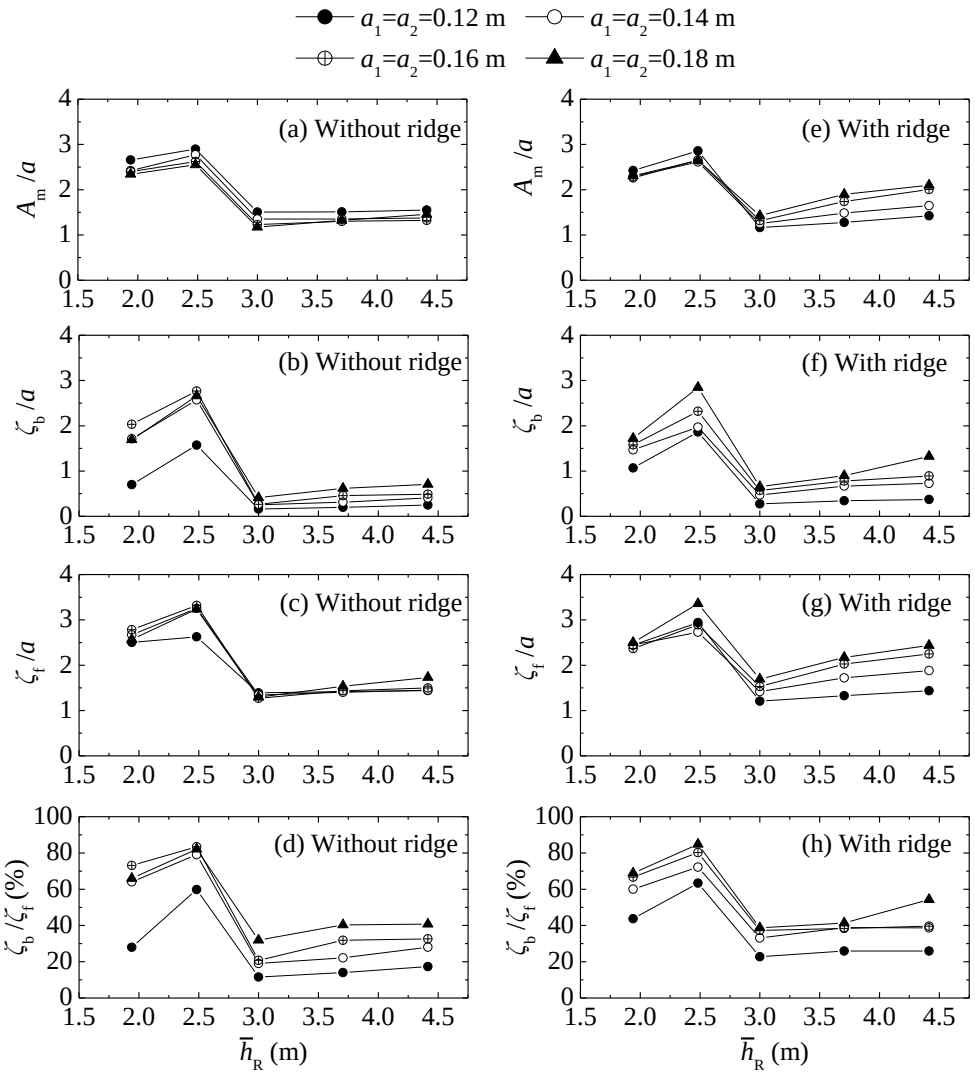

Fig. 14. Variations of the maximum IG period component amplitude, the separating amplitudes of the bound and the free IG waves and their relative components with respect to the mean water depth over the reef face with b=50.0 m. (a)–(d) correspond to the cases without the ridge, and (e)–(h) correspond to the cases with the ridge.

Fig. 15 illustrates the variations of the maximum IG period component amplitude, the separating amplitudes of the bound and the free IG waves and their relative components with respect to the mean water depth over the reef face, $\bar{h}_R$, under the condition of b=100.0 m. It can be easily found that the phenomena shown in this figure are similar to those shown in Fig. 14. That is, all the four variables shown in this figure tend to increase first, then decrease, and then increase again with the increasing of $\bar{h}_R$, and all of them get the maximum and minimum values when $\bar{h}_R$ =2.48 m and $\bar{h}_R$ =3.00 m, respectively. These phenomena are also different from the corresponding findings in Gao et al. (2017b) that when b=100.0 m, the bound IG wave amplitude decreases gradually with the increasing of $\bar{h}_R$, the free IG wave amplitude decreases first and then increases with $\bar{h}_R$, and the amplitude ratio, ζ_b/ζ_f, increases first and then decreases with $\bar{h}_R$.

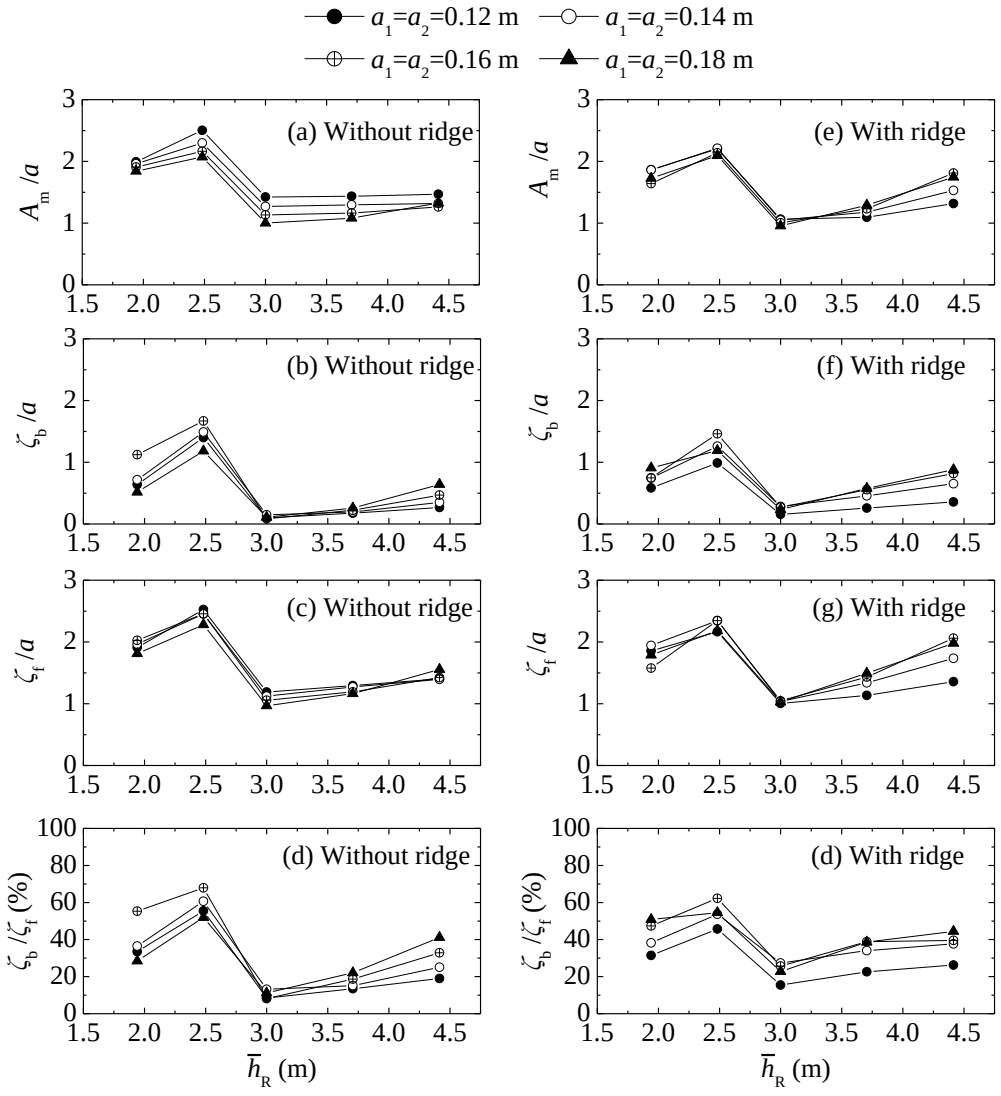

Fig. 15. Variations of the maximum IG period component amplitude, the separating amplitudes of the bound and the free IG waves and their relative components with respect to the mean water

depth over the reef face with b=100.0 m. (a)–(d) correspond to the cases without the ridge, and (e)–(h) correspond to the cases with the ridge.

4.5. Effect of the reef ridge on IG period waves

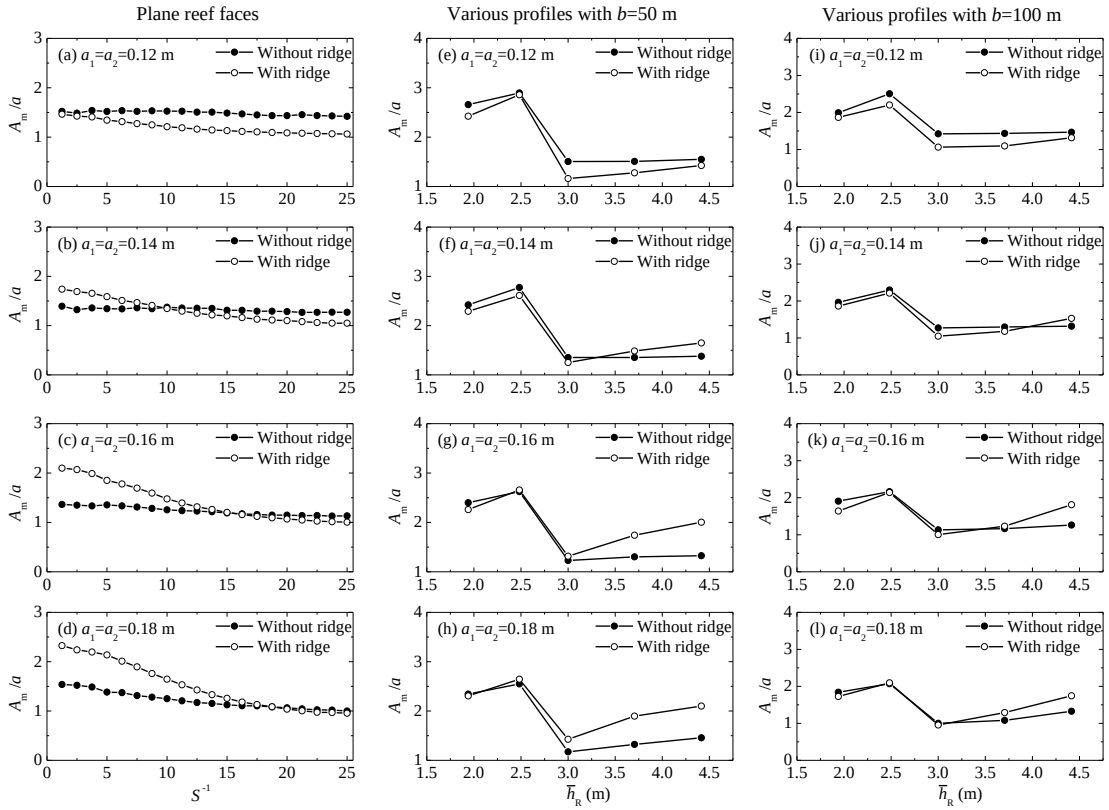

Fig. 16. Comparisons of the maximum IG period component amplitudes, A_m, under the two conditions of the existence of the reef ridge and no reef ridge. (a)–(d) correspond to the cases with plane reef faces; (e)–(h) and (i)–(l) correspond to the cases with various reef-face profiles under the conditions of b=50.0 m and 100.0 m, respectively.

Fig. 16 shows the comparisons of the maximum IG period component amplitudes, A_m, under the two conditions of the existence of the reef ridge and no reef ridge. When the harbor is exposed to the incident primary waves with the smallest amplitudes, i.e. a_1=a_2=0.12 m, the idealized reef ridge used in this paper restrains the maximum IG period component amplitude inside the harbor to some extent (Fig. 16a, e and i). However, as the incident primary wave amplitudes increase, the existence of the reef ridge gradually enhances the maximum IG period component amplitude

inside the harbor. When the incident primary wave amplitudes increase to a_1=a_2=0.18 m, the value of A_m with the reef ridge has become to approach or even remarkably exceed the corresponding one without reef ridge (Fig. 16d, h and l).

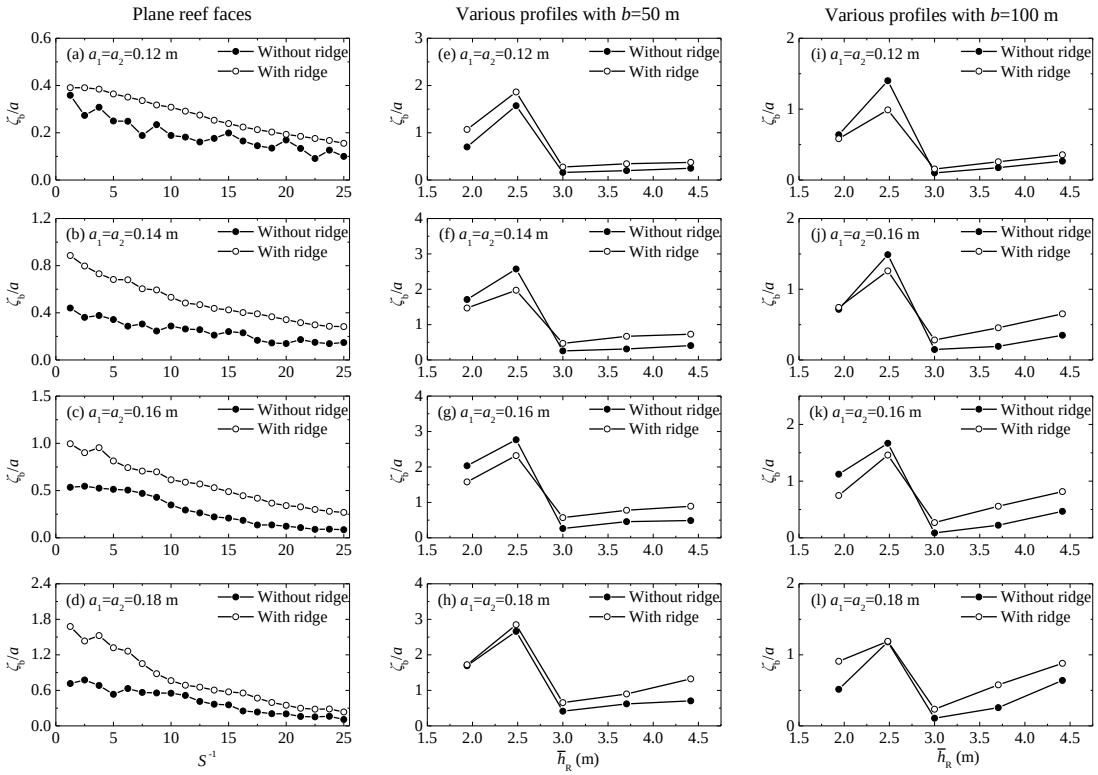

Fig. 17. Comparisons of the bound IG wave amplitudes, ζ_b, under the two conditions of the existence of the reef ridge and no reef ridge. (a)–(d) correspond to the cases with plane reef faces; (e)–(h) and (i)–(l) correspond to the cases with various reef-face profiles under the conditions of b=50.0 m and 100.0 m, respectively.

Fig. 17 presents the comparisons of the bound IG wave amplitudes, ζ_b, under the two conditions of the existence of the reef ridge and no reef ridge. For the reef face with plane slopes (Fig. 17a-d), it is seen that for all the incident primary wave amplitudes considered in this paper, the existence of the reef ridge significantly enhances the bound IG waves inside the harbor. However, for various reef-face profiles with b=50.0 m and b=100.0 m (Fig. 17e-l), the same phenomenon only can be observed in the cases in which the mean water depth over the reef face, $\bar{h}_R$, is equal to or larger than 3.0 m. For the cases in which $\bar{h}_R$ is less than 3.0 m, the influence of the reef ridge on the bound IG waves inside the harbor depends on both the incident primary wave

amplitudes and the mean water depth over the reef face, and no obvious variation trend can be observed. These phenomena are completely opposite to the corresponding findings in Gao et al. (2017b) that the existence of the reef ridge can restrain the bound IG waves inside the harbor to some extent for all the five reef-face topographies shown in Fig. 6.

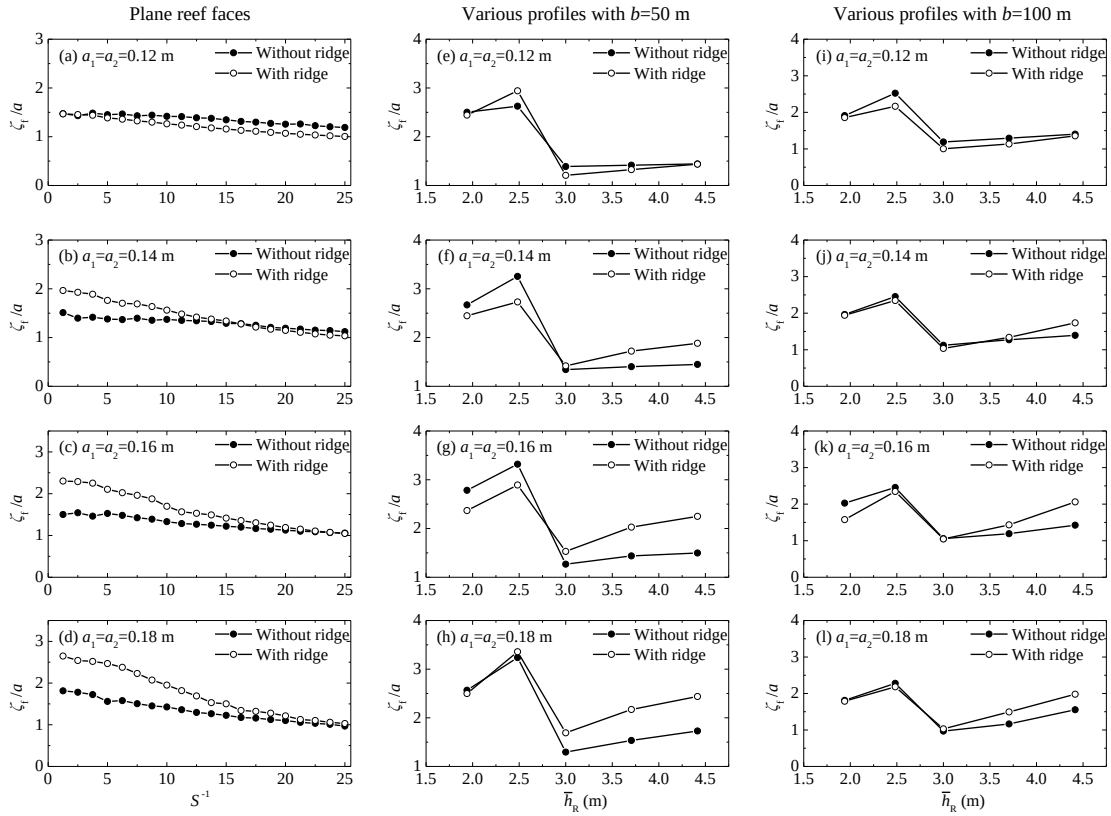

Fig. 18. Comparisons of the free IG wave amplitudes, ζ_f, under the two conditions of the existence of the reef ridge and no reef ridge. (a)–(d) correspond to the cases with plane reef faces; (e)–(h) and (i)–(l) correspond to the cases with various reef-face profiles under the conditions of b=50.0 m and 100.0 m, respectively.

Fig. 18 demonstrates the comparisons of the free IG wave amplitudes, ζ_f, under the two conditions of the existence of the reef ridge and no reef ridge. For the reef face with plane slopes (Fig. 18a-d), when the harbor is exposed to the incident primary waves with the smallest amplitudes (i.e. a_1=a_2=0.12 m), the reef ridge suppresses the free IG waves inside the harbor to some extent. As the incident primary wave amplitudes increase, the existence of the reef ridge gradually strengthens the free IG waves inside the harbor. When the incident primary wave

amplitudes increase to a_1=a_2=0.18 m, the value of ζ_f with the reef ridge fully exceeds the corresponding one without reef ridge. These phenomena are very similar with those for the maximum IG period component amplitude shown in Fig. 16. While for various reef-face profiles with b=50.0 m and b=100.0 m (Fig. 18e-l), the same phenomenon only can be observed in the cases in which the mean water depth over the reef face, $\bar{h}_R$, is equal to or larger than 3.0 m. For the cases in which $\bar{h}_R$ is less than 3.0 m, the influence of the reef ridge on the free IG waves inside the harbor depends on not only the incident primary wave amplitudes but also the mean water depth over the reef face, and no obvious variation trend can be observed. These phenomena mentioned above are different from the corresponding findings in Gao et al. (2017b) that the reef ridge has little influence on the free IG waves inside the harbor.

5. Conclusions

The IG period oscillations inside a long and narrow harbor near the offshore fringing reef excited by bichromatic primary waves with slightly different frequencies are simulated by utilizing the FUNWAVE 2.0 model. The IG wave analysis technique proposed by Dong et al. (2013) is employed to decompose the IG period components inside the harbor into bound and free IG waves. Effects of the plane reef-face slope, the reef-face profile shape and the existence of the reef ridge on the maximum IG period component amplitudes, the bound and the free IG waves and their relative components inside the harbor are systematically studied. Compared to the previous study in Gao et al. (2017b), the current research utilizes much larger incident bichromatic primary waves and wave breaking occurs over the fringing reef. The results of this investigation will enhance the knowledge of the influences of offshore fringing reefs on the IG period oscillations inside the harbor excited by the short wave groups.

The following conclusions can be drawn from the results of the present study:

1. For all the four incident primary wave amplitudes considered in this paper, the reef-face slope has remarkable effects on the maximum IG period component amplitudes, the bound and the free IG waves and their relative components inside the harbor. In general, all the four variables always increase gradually with the increasing of the reef-face slope, S, regardless of the incident primary wave amplitudes and whether the reef ridge exists or not.
2. For both the two reef-face widths considered in this paper, that is, b=50.0 m and 100.0 m, the reef-face profile shapes have notable and similar influences on the maximum IG period

component amplitudes, the bound and the free IG waves and their relative components inside the harbor. All the four variables tend to increase first, then decrease, and then increase again with the increasing of the mean water depth over the reef face, $\bar{h}_R$, regardless of the incident primary wave amplitudes and whether the reef ridge exists or not. Besides, all of the four variables always get the minimum values when $\bar{h}_R$ =3.00 m. Hence, from the viewpoint of the engineering application, the reef face with plane slope can restrain the IG period components inside the harbor to the most extent, compared to other profile shapes over the reef face.

3. The main influence of the reef ridge on the bound IG waves inside the harbor lies in that when the reef-face profile shapes have relatively large mean water depth ($\bar{h}_R \geq 3.0$ m), the existence of the reef ridge always significantly enhances the bound IG waves inside the harbor. As for the maximum IG period component amplitude and the free IG waves inside the harbor, its influences on both of them depend on the incident primary wave amplitudes.

Finally, we reaffirm here that these conclusions are only valid for the given harbor and reef ridge, the reef-face profile shapes and the variation ranges of the reef-face slopes and the incident primary wave amplitudes studied in this paper.

Acknowledgments

This work was financially supported by the National Natural Science Foundation of China (Grant no. 51609108), the Natural Science Foundation of the Jiangsu Higher Education Institutions of China (Grant no. 16KJB570004) and the Jiangsu Government Scholarship for Overseas Studies (awarded to Dr. Junliang Gao for study abroad at the University of Bath).

References

Bowers, E.C., 1977. Harbour resonance due to set-down beneath wave groups. Journal of Fluid Mechanics 79, 71-92.

Chawla, A., Kirby, J.T., 2000. A source function method for generation of waves on currents in Boussinesq models. Applied Ocean Research 22 (2), 75-83.

De Jong, M.P.C., Battjes, J.A., 2004. Seiche characteristics of Rotterdam Harbour. Coastal Engineering 51 (5-6), 373-386.

Dong, G., Chen, H., Ma, Y., 2014. Parameterization of nonlinear shallow water waves over

sloping bottoms. Coastal Engineering 94, 23-32.

Dong, G., Gao, J., Ma, X., Wang, G., Ma, Y., 2013. Numerical study of low-frequency waves during harbor resonance. Ocean Engineering 68, 38-46.

Dong, G., Wang, G., Ma, X., Ma, Y., 2010. Harbor resonance induced by subaerial landslide-generated impact waves. Ocean Engineering 37 (10), 927-934.

Fabrikant, A.L., 1995. Harbor oscillations generated by shear flow. Journal of Fluid Mechanics 282, 203-217.

Gao, J., Ji, C., Gaidai, O., Liu, Y., 2016a. Numerical study of infragravity waves amplification during harbor resonance. Ocean Engineering 116, 90-100.

Gao, J., Ji, C., Gaidai, O., Liu, Y., Ma, X., 2017a. Numerical investigation of transient harbor oscillations induced by N-waves. Coastal Engineering 125, 119-131.

Gao, J., Ji, C., Liu, Y., Gaidai, O., Ma, X., Liu, Z., 2016b. Numerical study on transient harbor oscillations induced by solitary waves. Ocean Engineering 126, 467-480.

Gao, J., Ji, C., Liu, Y., Ma, X., Gaidai, O., 2017b. Influence of offshore topography on the amplification of infragravity oscillations within a harbor. Applied Ocean Research 65, 129-141.

Gao, J., Ji, C., Liu, Y., Ma, X., Gaidai, O., 2018. Numerical study on transient harbor oscillations induced by successive solitary waves. Ocean Dynamics 68 (2), 193-209.

Gao, J., Ji, C., Ma, X., Liu, Y., Gaidai, O., 2017c. Numerical investigation of infragravity wave amplifications during harbor oscillations influenced by variable offshore topography. Ocean Dynamics 67 (9), 1151-1162.

González-Marco, D., Sierra, J.P., Ybarra, O.F.d., Sánchez-Arcilla, A., 2008. Implications of long waves in harbor management: The Gijón port case study. Ocean & Coastal Management 51 (2), 180-201.

Guerrini, M., Bellotti, G., Fan, Y., Franco, L., 2014. Numerical modelling of long waves amplification at Marina di Carrara Harbour. Applied Ocean Research 48, 322-330.

Kirby, J.T., Long, W., Shi, F., 2003. Funwave 2.0 Fully Nonlinear Boussinesq Wave Model On Curvilinear Coordinates. Report No. CACR-02-xx. Center for Applied Coastal Research, Dept. of Civil & Environmental Engineering, University of Delaware, Newark, Delaware.

Kumar, P., Gulshan, 2017. Extreme Wave-Induced Oscillation in Paradip Port Under the

Resonance Conditions. Pure and Applied Geophysics DOI 10.1007/s00024-017-1646-3.

Kumar, P., Zhang, H., Kim, K.I., 2014. Spectral Density Analysis for Wave Characteristics in Pohang New Harbor. Pure and Applied Geophysics 171, 1169-1185.

Kumar, P., Zhang, H., Kim, K.I., Yuen, D.A., 2016. Modeling wave and spectral characteristics of moored ship motion in Pohang New Harbor under the resonance conditions. Ocean Engineering 119, 101-113.

Longuet-Higgins, M.S., Stewart, R.W., 1962. Radiation stress and mass transport in gravity waves, with application to 'surf beat'. Journal of Fluid Mechanics 13 (4), 481-504

López, M., Iglesias, G., 2013. Artificial intelligence for estimating infragravity energy in a harbor. Ocean Engineering 57, 56-63.

Ma, Y., Chen, H., Ma, X., Dong, G., 2017. A numerical investigation on nonlinear transformation of obliquely incident random waves on plane sloping bottoms. Coastal Engineering 130, 65-84.

Mei, C.C., 1983. The Applied Dynamics of Ocean Surface Waves. Wiley, New York.

Nwogu, O., Demirbilek, Z., 2010. Infragravity wave motions and runup over shallow fringing reefs. Journal of Waterway, Port, Coastal, and Ocean Engineering 136 (6), 295-305.

Rabinovich, A.B., 2009. Seiches and harbor oscillations, in: Kim, Y. (Ed.), Handbook of Coastal and Ocean Engineering. World Scientific Publishing, Singapore, pp. 193-236.

Rogers, S.R., Mei, C.C., 1978. Nonlinear resonant excitation of a long and narrow bay. Journal of Fluid Mechanics 88 (1), 161-180.

Shi, F., Dalrymple, R.A., Kirby, J.T., Chen, Q., Kennedy, A., 2001. A fully nonlinear Boussinesq model in generalized curvilinear coordinates. Coastal Engineering 42, 337-358.

Thotagamuwage, D.T., Pattiaratchi, C.B., 2014. Influence of offshore topography on infragravity period oscillations in Two Rocks Marina, Western Australia. Coastal Engineering 91, 220-230.

Wei, G., Kirby, J.T., Grilli, S.T., Subramanya, R., 1995. A fully nonlinear Boussinesq model for surface waves. Part 1. Highly nonlinear unsteady waves. Journal of Fluid Mechanics 294, 71-92.

Yao, Y., Becker, J.M., Ford, M.R., Merrifield, M.A., 2016. Modeling wave processes over fringing reefs with an excavation pit. Coastal Engineering 109, 9-19.

Yao, Y., He, F., Tang, Z., Liu, Z., 2018. A study of tsunami-like solitary wave transformation and run-up over fringing reefs. Ocean Engineering 149, 142-155.